Peculiarities of axial and radial Ge–Si heterojunction formation in nanowires: Monte Carlo simulation*

Nataliya L. Shwartz‡, Alla G. Nastovjak, and Igor G. Neizvestny

A.V. Rzhanov Institute of Semiconductor Physics SB RAS, Novosibirsk, Russia

Abstract: The process of axial and radial Si–Ge heterostructure formation during nanowire growth by vapor–liquid–solid (VLS) mechanism was studied using Monte Carlo (MC) simulation. It was demonstrated that radial growth can be stimulated by adding chemical species that decrease the activation energy of precursor dissociation or the solubility of semiconductor material in catalyst drop. Reducing the Si adatom diffusion length also leads to Si shell formation around the Ge core. The influence of growth conditions on the composition and abruptness of axial Ge–Si heterostructures was analyzed. The composition of the Ge_xSi_{1-x} axial heterojunction (HJ) was found to be dependent on the flux ratio, the duration of Si and Ge deposition, and the catalyst drop diameter. Maximal Ge concentration in the HJ is dependent on Ge deposition time owing to gradual changing of catalyst drop composition after switching Ge and Si fluxes. The dependence of junction abruptness on the nanowire diameter was revealed: in the adsorption-induced growth mode, the abruptness decreased with diameter, and in the diffusion-induced mode it increased. This implies that abrupt Ge–Si HJ in nanowires with small diameter can be obtained only in the chemical vapor deposition (CVD) process with negligible diffusion component of growth.

Keywords: germanium; heterojunctions; Monte Carlo simulation; nanowires; semiconductors; silicon; simulation.

INTRODUCTION

Semiconductor nanowires or nanowhiskers (NWs) with heterojunctions (HJs) have great potential in future electronics, optoelectronics, and medicine [1,2]. Semiconductor nanowires are interesting objects for investigation of the low-dimensional effects such as charge carrier quantum confinement, modification of band structure, and the crystal phase [1,3,4]. It is possible to form axial and radial junctions in nanowires using different materials (Si–Ge, GaAs–AlGaAs, GaAs–GaP, and others) [5–12]. Superlattices on the base of whiskers with axial HJs may be used as injection lasers, 1D waveguides, etc. [13,14]. Radial heterostructures are the platform for unique devices, such as effective emitters, nanowire field-effect transistors with promising device performance and building blocks to form solid-state qubits [15–18]. Ge–Si NWs are of particular interest owing to their compatibility with traditional Si technology. Variation of Ge_xSi_{1-x} NW composition gives possibilities to change the lattice constant, energy band gap, mobility, and some other physical properties of materials [19,20]. HJs in nanowires can be formed directly during the NW growth and do not require additional technological steps as com-

pared with planar device structures. In general, NWs are formed via vapor–liquid–solid (VLS) growth activated by Au catalyst [21]. Au is attractive because of its ability to form low-temperature eutectic binary alloys. Eutectic temperatures for Si–Au and Ge–Au binary alloys are 363 and 361 °C with different alloy composition in eutectic point: Si and Ge percentages are 18.6 and 28.0 atom %, respectively [22]. Binary alloy composition depends on drop size as well on growing crystal shape [23,24].

To form HJs, the sources of deposited materials are switched during the NW growth process. Usually, core-shell Ge–Si heterostructures are formed as follows: Ge core grown via VLS mechanism is covered with uniform Si shell. Simple precursor switching from Ge-containing precursors to Si-containing precursors does not result in Si shell growth. Instead, axial NW elongation occurs [11]. There are several experimental works demonstrating radial core-shell Ge–Si and Si–Ge heterostructure formation, with radial shell growth turned on by variation of temperature, gas composition, and pressure or by removing catalyst drop [9,25–29]. In [26], radial shell growth was "turned on" by the addition of diborane, which serves to lower the decomposition temperature of silane. Based on experimental work [30] where diboran introduction in the growth chamber results in an increase in the polysilicon film growth rate, diboran was believed to enhance the precursor dissociation rate [26]. However, impurity (boron) could also change Si solubility in the catalyst drop or change the Si surface diffusion length. In spite of progress in core-shell structure formation, the exact limitations of such growth have not been fully understood.

The main parameters of HJs are their abruptness and composition. Experimental Si–Ge axial HJs in VLS-grown NWs are not atomically flat [5,6]. The HJ blurriness appeared to be due to principal restrictions of the VLS growth mechanism [31]. Therefore, in recent papers Al–Au with high eutectic temperature [32] was suggested as catalyst. The increase of eutectic temperature leads to transition from VLS growth mechanism to a VSS (vapor–solid–solid) one [33]. That allows growing abrupt HJ. Using Au–Ga catalyst drop with low Ge concentration in the alloy, sharp Si–Ge junctions were formed [34]. Characteristics of HJs in VLS-grown NWs depend to a large extent on catalyst drop composition. Experimental in situ observation of drop composition is a rather complicated task, and thus simulation is suitable for investigating the drop and HJ compositions and NW growth kinetics. In this work, various factors that have an effect on the width of axial Ge–Si HJs in VLS-grown silicon NWs and on Ge–Si core-shell NW formation were analyzed using Monte Carlo (MC) simulation. The effect of precursor type, flux intensity, and temperature on the transition from axial to radial heterogrowth was investigated. The dependences of axial HJ abruptness on NW diameter, flux intensity, solubility of semiconductor material in catalyst drop and duration of Ge deposition were obtained.

MONTE CARLO MODEL

Simulation was carried out using the lattice MC model [35]. The following elementary events for particles were considered in the model: adsorption, diffusion hop, desorption, and chemical reactions. The probability of each event exponentially depends on activation energy. Earlier we realized the MC model of single-component NW growth [36]. NWs grew from semiconductor material deposited on the diamond-like crystal lattice substrate with (111) orientation activated by catalyst drop. Particles (atoms or molecules) from the flux could be deposited perpendicular to the substrate, or at arbitrary angles imitating the vapor phase. Semiconductor material arrives at the drop directly from the flux and by diffusion via the substrate surface. NWs grew because of: (1) dissolution of the semiconductor material in the drop with following crystallization at the drop–whisker interface; (2) atom incorporation along triple VLS line at sites provided with incomplete wetting. The input parameters of the model are composition, orientation, and morphology of initial substrate, energy of covalent bonds E_{i-j} (i, j = matter sorts), activation energies of chemical reactions (E_r) and desorption (E_{sub}), temperature T (K), flux intensity F (monolayer/s = ML/s). One can find details of model realization elsewhere [36].

The scheme of the model process is presented in the following way. Silicon atoms, Si(s), were dissolved into the Au drop according to the reaction: Si(s) + Au → Si(liq) + Au (E_r = 2.7 eV), where Si(s) and Si(liq) = solid- and liquid-phase Si, respectively. As in experimental work [37], irreversible precursor dissociation was considered in this work. That is the mean semiconductor atom cannot come back into the gas phase. Si diffusion through the drop was simulated by the reaction Si(liq) + Au → Au + Si(liq) (E_r = 3.7 eV). Si(liq) crystallized only when contacting with solid-phase Si: Si(liq) + Si(s) → Si(s) + Si(s) (E_r = 2.6 eV). The VLS process for Ge was the same. If Si and Ge are deposited simultaneously, semiconductor crystallization may occur when contacting the solid phase of both semiconductors: Si(liq) + Ge(s) → Si(s) + Ge(s) and Ge(liq) + Si(s) → Ge(s) + Si(s), where Ge(s) and Ge(liq) = solid- and liquid-phase Ge, respectively. Figure 1 schematically illustrates the atomic processes in catalyst drop and at the semiconductor–catalyst interface.
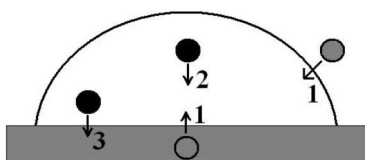
Fig. 1 Atomic processes in catalyst drop: (1) Si(s) dissolution into the drop; (2) Si(liq) exchange diffusion in the drop; (3) Si(liq) crystallization. Si(s) is marked in gray, Au in white, and Si(liq) in black.

Dissolution and crystallization occurring at the liquid–solid interface play a decisive role in eutectic alloy formation. When the system is at equilibrium, the rates of these processes are equal: V_{dissol} = V_{cr}. From this expression, one can find equilibrium concentration of liquid Si in Si–Au alloy: $C_{Si(liq)}$ = $K_{0dissol}/K_{0cr}\cdot\exp[-(E_{dissol} - E_{cr})/kT]\cdot C_{Au}$, where $K_{0dissol}$ and K_{0cr} = pre-exponential factors of dissolution and crystallization rate constants, E_{dissol} and E_{cr} = activation energies of these processes and C_{Au} = Au concentration. In accordance with the Si–Au binary-phase alloy diagram [22], $C_{Si(liq)}$ should increase with temperature and consequently the following relation should be true: $E_{dissol} > E_{cr}$.

The relationship $E_{Ge-Ge} < E_{Si-Si} < E_{Si-Ge}$ was chosen for Si–Ge surface bonds on the base of island density in Si–Si, Si–Ge, and Ge–Ge systems [38–40]. Simulation was carried out using the following energies of covalent bonds: E_{Si-Si} = 1 eV, E_{Si-Ge} = 1.2 eV, E_{Ge-Ge} = 0.95 eV, $E_{Au-Si} = E_{Au-Ge}$ = 0.6 eV, E_{Au-Au} = 1 eV. The effect of Si–Ge mechanical strain on the bond energies was not taken into account because the ratio of whisker surface to the bulk is large enough, resulting in the effective strain relaxation [41].

To simulate radial HJ growth, a seven-component system was considered: substrate and wire material Si(s); wire material Ge(s); catalyst (Au); Si- and Ge-containing precursors (P_{Si} and P_{Ge}); liquid semiconductor materials dissolved in catalyst drop [Si(liq) and Ge(liq)]. For simulation axial HJ molecular beam epitaxy (MBE) growth 5-component system was enough: Si(s), Ge(s), Si(liq), Ge(liq), Au.

SIMULATION RESULTS AND DISCUSSION

Since parameters of Si–Ge HJs grown in NWs via VLS mechanism are determined by catalyst drop composition, the model dependences of Si concentration $C_{Si(liq)}$ in catalyst drop on temperature, flux intensities, and initial drop diameter were obtained. We analyzed the temperature dependence of equilibrium (without flux) and nonequilibrium (under the flux) steady-state concentration $C_{Si(liq)}$. After annealing of the Si substrate with Au drop under temperatures of 720–850 K, Si concentration in the drop was changed from 17 to 20 atom %. NW growth at the same temperatures results in higher Si concentration in Au–Si alloy because external Si flux leads to the drop supersaturation. The increase of

equilibrium and nonequilibrium $C_{Si(liq)}$ with drop diameter decreasing (d = 3.6–9.6 nm) was observed. Figure 2 illustrates variation of Si concentration in Au drop with time during NW growth. One can see evident oscillations of concentration near some average values. These oscillations are not random fluctuations and are directly associated with the crystallization process. Mean concentration value is the nonequilibrium concentration stabilized in the drop of given diameter under given growth conditions. Curve maximums correspond to supersaturation required for crystallization at the drop–whisker interface to start. After starting crystallization, Si concentration in the drop decreases until one complete bilayer of semiconductor matter will not be formed under the drop (this moment corresponds to curve minimums). The insert in Fig. 2a demonstrates cross-sections of the drop–whisker interface near maximum and minimum of the curve. At the maximum, the new layer nucleates, and at the minimum it finishes to form. We analyzed dependences of concentration oscillation period on drop diameter, temperature, and flux intensity. The oscillation period rises with diameter enhancement owing to the increase of crystallization time (time necessary to complete new layer formation at the drop–NW interface). Besides that, the process of Si accumulation to achieve supersaturation in the liquid drop slows down for larger drop diameter. The flux increase results in shortening of the oscillation period (Fig. 2b) owing to decreasing of Si(liq) accumulation time. For considered temperature diapason, the oscillation period does not depend on temperature, but mean Si(liq) concentration in the drop increases with T. The above dependences correspond to the Si–Au binary system, but they are similar for Ge–Au.
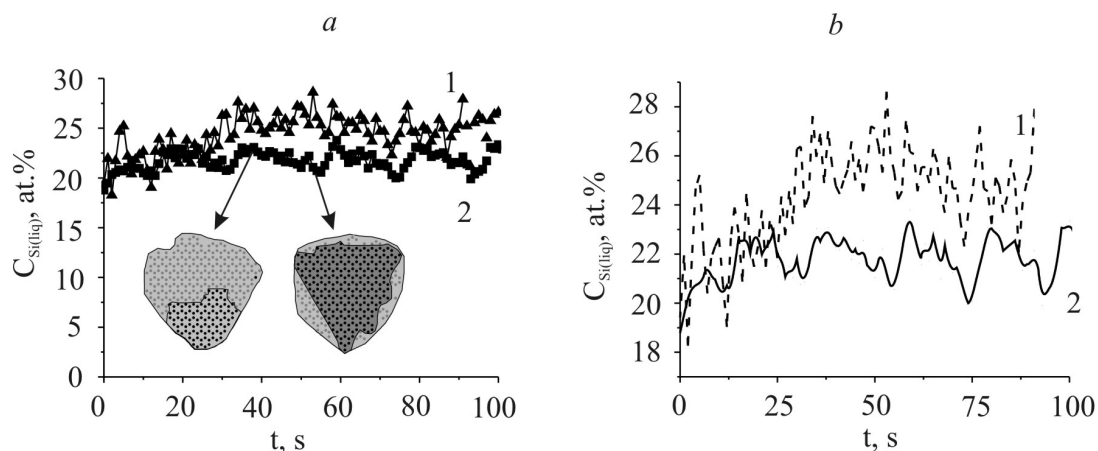

Fig. 2 Variation of Si concentration $C_{Si(liq)}$ with time at T = 800 K: (a) d = 3.6 nm (1), 9.6 nm (2), F = 0.01 ML/s; (b) d = 6 nm, F = 0.1 ML/s (1), 0.02 ML/s (2). Insert shows drop–whisker interface cross-sections at the moments indicated by arrows.

Radial Ge–Si heterojunctions

The process of Ge–Si core-shell NW formation was analyzed. As the first step, on the Si(111) substrate activated by the Au drop, Ge-containing precursors were deposited. So Ge core growth via VLS mechanism was simulated. The next step was Si shell formation. Since simple precursor switching from P_{Ge} to P_{Si} does not result in Si shell growth, introduction of additional species in the system provoking radial growth was considered. There are several reasons for Si shell formation when adding impurities.

Impurity can modify the activation energy of precursor dissociation. We analyzed the effect of precursor dissociation activation energy E_{dissP} on radial growth rate V. Figure 3a demonstrates this dependence: the radial growth rate increases with E_{dissP} decreasing. In Fig. 3b, cross-sections of model Ge–Si core-shell structure are shown for two E_{dissP} values: 1 and 0.3 eV. Images (1) and (2) correspond
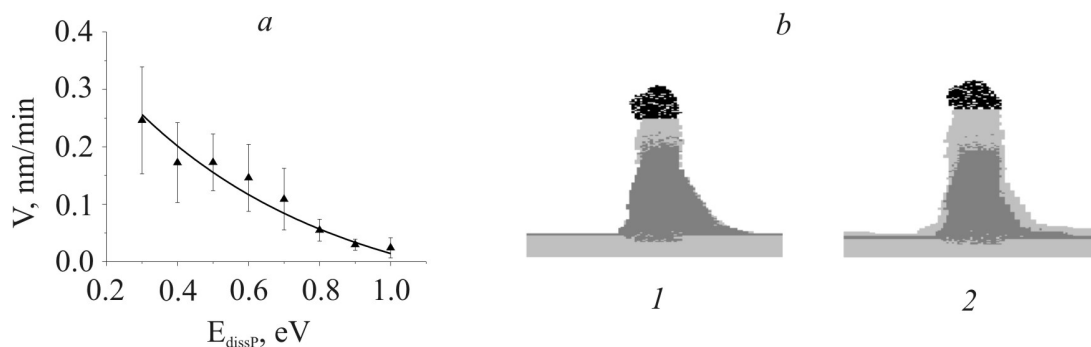
Fig. 3 (a) Radial growth rate of Si shell vs. activation energy of precursor dissociation E_{dissP} at $T = 800$ K; (b) cross-sections of Ge–Si core-shell NW for E_{dissP} 1.0 eV (1) and 0.3 eV (2); $\tau_{Si} = 100$ s. Si is marked in light gray, Ge in dark gray, Au in black, and Si(liq), Ge(liq) in white.

to the same deposition time τ of Si precursor. At high E_{dissP}, radial growth is practically lacked, and at low E_{dissP}, Si shell formation is clearly seen. The introduction of an additional chemical component can influence not only the precursor dissociation rate but also the catalyst drop properties. We consider the effect of impurities on Si solubility in the catalyst drop. The dissolution rate of Si in catalyst drop in the model was determined by activation energy E_r of the reaction Si(s) + Au → Si(liq) + Au. Figures 4a,b demonstrate the influence of E_r value on the Si shell thickness. The value $E_r = 2.7$ eV corresponds to the VLS growth mechanism when the axial HJ is formed. In this case, P_{Si} deposition leads to Si fragment of NW growth, with Si shell thickness being negligible. For $E_r = 5$ eV, Si is practically insoluble in catalyst drop and precursor dissociation results in the increase of Si atom concentration on the NW wall surface, initiating Si shell formation. Moreover, some impurities being surfactants can decrease Si adatom diffusion length L_{diff} and so provoke shell growth. L_{diff} is determined by binding energy between the Si atom and the core atoms. For example, for such an impurity as boron, the binding energy $E_{Si–B}$ is higher than $E_{Si–Ge}$ [42]. So doping of growing whiskers by boron should decrease Si diffusion length along NW walls leading to radial growth. The influence of Si-impurity binding energy E_{Si-imp} on the shell formation process is illustrated by Figs. 4c,d: $E_{Si–Ge} = 1.2$ eV, $E_{Si-imp} = 1.5$ eV, so $L_{diff\_Si-imp} < L_{diff\_Si–Ge}$.
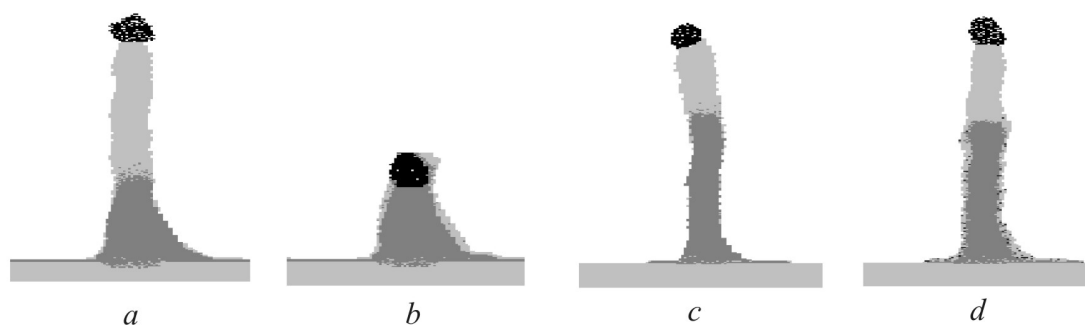

Fig. 4 Cross-sections of Ge–Si core-shell NW for different Si solubility in catalyst drop (a,b) and different Si diffusion length along NW surface (c,d) at $T = 800$ K, $\tau_{Ge} = 500$ s, $\tau_{Si} = 360$ s, $F_{Ge} = 0.05$ ML/s, $F_{Si} = 0.05$ ML/s, $d = 6$ nm: (a) $E_r = 2.7$ eV; (b) $E_r = 5.0$ eV (E_r = activation energy responsible for Si dissolution in catalyst drop); (c) growth without impurity; (d) $F_{imp} = 0.005$ ML/s, $E_{Si-imp} = 1.5$ eV. Si(s) is marked in light gray, Ge(s) in dark gray, Au in black, and Si(liq), Ge(liq) in white.

Axial Ge–Si heterojunctions

To imitate MBE growth of axial Ge–Si HJ, fluxes of atomic Si and Ge (F_{Si} and F_{Ge}, correspondingly) were switched alternately to grow Si and Ge parts of the whisker. Growth conditions were chosen in accordance with experimental work [5]. The typical values of the fluxes were $F_{Si} = 0.05$ ML/s and $F_{Ge} = 0.01$ ML/s. The growth temperature was constant during the deposition of both Si and Ge and equal to 800 K. The growth duration of the first Si segment, τ_{Si}, was 200 s with duration of Ge deposition varying in the range of 20–200 s. The range of drop diameter ($d = 3.6$–12 nm) was lower than in the experiment.

Figure 5a shows the model whisker with axial HJs. Thin Ge layers were embedded into Si NW during the growth. The Ge concentration profile along the NW axis is shown in Fig. 5b. One can see that the interface between Si and Ge segments is not abrupt, with the embedded layer composition being $Ge_x Si_{1-x}$. Figure 6a demonstrates Ge concentration profiles for various Ge deposition times: $\tau_{Ge} = 20$, 100, and 200 s. The longer the deposition time, the higher maximal Ge concentration is reached in the grown layer. At fixed τ_{Ge}, the maximal Ge concentration x_{max} in the Ge fragment of whisker increases with Ge flux intensity (Fig. 6b). The dependence of x_{max} on the NW diameter is shown in Fig. 6c. NW growth occurs via dissolution of deposited material in the catalyst drop and following crystallization under the drop. Although switching of Si and Ge sources is instantaneous, the drop contains residual Si that will crystallize gradually together with Ge. This is the reason for nonabrupt Si–Ge HJ formation. Variation of Si(liq) and Ge(liq) concentration in the Au drop with time for different duration of Ge flux for two drop diameters is shown in Fig. 7. Figures 7a,b illustrate the kinetics of drop composition variation after flux switching. After the Ge source is turned on, liquid Si in catalyst drop is gradually replaced by Ge coming from the flux (Fig. 7c). The longer the τ_{Ge}, the lower Si percentage is in the drop. It results in higher Ge percentage in the growing layer. Drop composition kinetics was found to be dependent on drop diameter: the larger the diameter, the slower is the atomic substitution process. So maximal Ge concentration in the $Ge_x Si_{1-x}$ layer decreases with diameter increasing owing to the gradual change of catalyst drop composition after switching the fluxes.
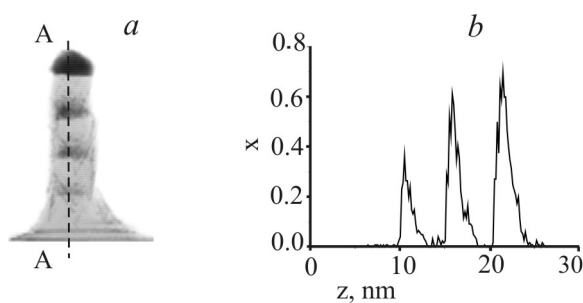
Fig. 5 (a) Si NW with three axial Ge layers: $F_{Si} = 0.05$ ML/s, $F_{Ge} = 0.01$ ML/s, $d = 6$ nm, duration of Ge layers deposition $\tau_{Ge1} = 20$ s, $\tau_{Ge2} = 40$ s, $\tau_{Ge3} = 60$ s; Si(s) is marked in light gray, Ge(s) in dark gray; (b) Ge concentration profile along A-A line, $x = $ Ge fraction in $Ge_x Si_{1-x}$ layer.
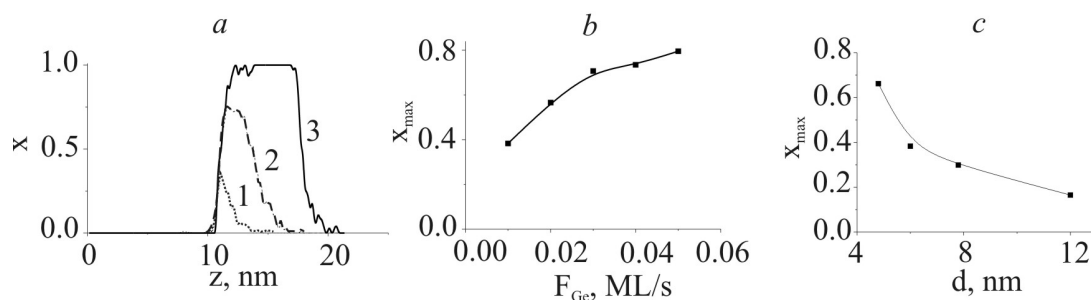
Fig. 6 (a) Ge concentration profile in Ge_xSi_{1-x} layer for different τ_{Ge} values: (1) 20 s, (2) 100 s, (3) 200 s ($d = 6$ nm, $F_{Si} = 0.05$ ML/s, $F_{Ge} = 0.01$ ML/s); maximal Ge concentration x_{max} in Ge_xSi_{1-x} layer vs. intensity of Ge flux for $d = 6$ nm, $\tau_{Ge} = 20$ s (b) and drop diameter (c) for $\tau_{Ge} = 20$ s, $F_{Ge} = 0.01$ ML/s.
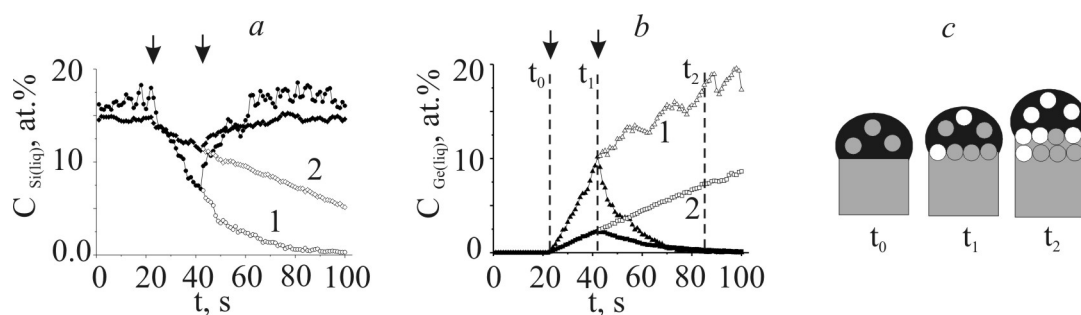
Fig. 7 Concentration Si(liq) (a) and Ge(liq) (b) in the drop vs. time for different diameters d_0 and duration of Ge deposition τ: (1) $d_0 = 6$ nm, (2) $d_0 = 12$ nm; $\tau_1 = 20$ s (solid marks), $\tau_2 = 100$ s (unshaded marks). Arrows indicate moments of fluxes switching; (c) illustrates atom substitution process in catalyst drop after flux switching (Si is marked in gray, Ge in white, and Au in black).

We investigated the effects of NW diameter, flux intensity, semiconductor solubility in catalyst and Ge deposition time on HJ abruptness in various growth modes. In Ge concentration profiles (Fig. 5b), one can see leading and trailing edges. The thickness of these regions corresponds to Si–Ge HJ width. In [31], the concentration in leading and trailing edges was fitted by decay exponential functions as $n_{Ge}(z) = n_0 - A \cdot \exp(-z/\alpha)$ and $n_{Ge}(z) = n_0 + B \cdot \exp(-z/\beta)$, where n_0 = Ge concentration after stabilization, A, B = constant coefficients, z = coordinate along the NW axis, α and β = coefficients characterizing the HJ width. But in [6] it was shown that the trailing edge is approximated by error function more accurately. As in [34], we estimated the width of the HJ as the distance over which Ge concentration changes from 10 to 90 % of the maximum value. Widths of the leading and trailing edges of the Ge profile were characterized by coefficients α and β, correspondingly. HJ width may be expressed as: $\alpha = V \cdot t_{st}$, where V = NW growth rate and t_{st} = time required for complete Ge substitution for Si in the catalyst drop (time required for saturation of Ge_xSi_{1-x} composition). In the general case, both V and t_{st} depend on the catalyst drop diameter. Figure 8a shows the dependence of t_{st} on NW diameter d. Previously, the growth rate was shown to be independent of the diameter in the adsorption-induced growth mode and to be proportional to $1/d$ or $1/d^2$ in the diffusion-induced mode [36]. In the diffusion-induced mode, NW growth occurs owing to matter diffusion flux from the substrate and in adsorption-induced mode owing to direct adsorption on the drop surface. Therefore, α is $\sim d$ for adsorption growth and is either independent of d or $\sim 1/d$ for diffusion growth. Relation $\alpha \sim 1/d$ is the theoretical prediction for NW growth by MBE because in MBE the diffusion component predominates. Figures 8b,c demonstrate the dependences of leading edge abruptness α on the NW diameter. In adsorption-induced
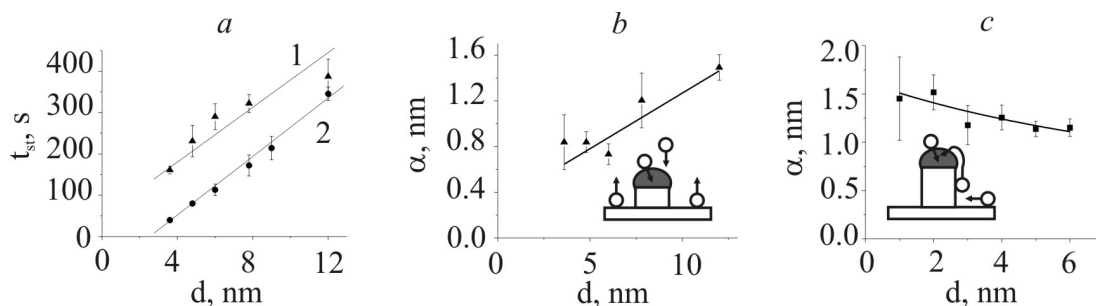
Fig. 8 (a) Time necessary to achieve composition saturation in Ge_xSi_{1-x} fragment of NW vs. diameter: in diffusion (1) and adsorption (2) growth modes; (b,c) dependence of HJ abruptness α on NW diameter in adsorption (b) and diffusion (c) growth modes. Inserts illustrate schemes of adsorption and diffusion regimes.

mode, HJ abruptness decreases with diameter and in diffusion-induced mode increases. If τ_{Ge} is shorter than t_{st}, HJ abruptness instead of α and β coefficients may be described by the half-width of Ge peak in the concentration profile. Analysis of simulation results demonstrated HJ abruptness to be independent of flux intensities. To sum up, in adsorption-induced growth mode, HJ abruptness is ~d (Fig. 8b), and in diffusion-induced mode it is the decreasing function of d (Fig. 8c). Increasing dependence $\alpha(d)$ was shown for CVD-grown NWs with axial Si–Ge HJs experimentally [6]. The authors of work [31] obtained $\alpha \sim d$, but they did not take into consideration $V(d)$ dependence. Careful analysis of $\alpha(d)$ dependence in [6] indicates that $\alpha \sim d^n$ ($n > 1$). In the same work, it was demonstrated that $V \sim d$ (for small d), so according to our arguments, HJ abruptness can be fitted as $\alpha \sim d^2$.

Though we discussed HJ abruptness of the leading edge, the obtained results qualitatively describe the trailing edge as well. Special computing experiment showed $\alpha = \beta$ if Si and Ge were supposed to be identical chemical elements. It agrees with the data of [31] where Si and Ge were considered as two isotopes of the same materials. In the present paper, all results were obtained taking into account some differences between Si and Ge: different values of covalent bond energies, solubility in Au, and surface tension of Si–Au and Ge–Au alloys. Our results are in accordance with [34] where it was demonstrated that semiconductor solubility in the catalyst drop had a crucial influence on HJ abruptness: the higher the solubility, the more blurred the HJ. In accordance with referenced data [22], Ge solubility in Au is higher than the Si solubility, that is why the trailing edge is less abrupt than the leading one ($\beta > \alpha$) (Fig. 5b). It agrees with experimental data for CVD growth of NWs with Si–Ge HJs [6] but is contradictory with the same MBE experiment [5]. This disagreement may be due to mechanical stresses that become more significant in thicker whiskers grown by MBE technique.

CONCLUSIONS

In this work, atomic-scaled analysis of axial Ge–Si heterostructure formation and Ge–Si core-shell NW growth was carried out using lattice MC model. Dependence of radial growth rate on the activation energy of precursor dissociation was obtained. It was demonstrated that decrease of the activation energy of Si precursor dissociation results in Si shell formation around the Ge core. Radial growth can be stimulated by adding chemical species that decrease the solubility of the semiconductor material in catalyst drop or decrease Si adatom diffusion. Dependences of maximal Ge concentration in axial Si–Ge junctions in Si whiskers on the ratio of Si and Ge flux intensities, duration of these fluxes, and Au drop diameter were obtained. Dependence of Ge percentage in the Ge_xSi_{1-x} layer on Ge deposition time is the result of a gradual change of liquid drop composition after switching the fluxes (phenomenon of residual concentration). This delay is the main reason for HJ blurriness. Junction abruptness was found to be dependent on NW diameter: in adsorption-induced growth mode, abruptness decreases with diameter, and in diffusion-induced mode it increases. This means that the abrupt Si–Ge HJ in nanowires

with small diameter can be obtained only in the CVD process with a negligible diffusion component of growth.

ACKNOWLEDGMENT

REFERENCES

1. O. Hayden, R. Agarwal, W. Lu. *Nano Today* **3**, 12 (2008).
2. Y. Li, F. Qian, J. Xiang, C. M. Lieber. *Mater. Today* **9**, 18 (2006).
3. J.-S. Park, B. Ryu, C.-Y. Moon, K. J. Chang. *Nano Lett.* **10**, 116 (2010).
4. J. Johansson, K. A. Dick, P. Caroff, M. E. Messing, J. Bolinsson, K. Deppert, L. Samuelson. *J. Phys. Chem. C* **114**, 3837 (2010).
5. N. D. Zakharov, P. Werner, G. Gerth, L. Schubert, L. Sokolov, U. Gosele. *J. Cryst. Growth* **290**, 6 (2006).
6. T. E. Clark, P. Nimmatoori, K.-K. Lew, L. Pan, J. M. Redwing, E. C. Dickey. *Nano Lett.* **8**, 1246 (2008).
7. R. Dujardin, V. Poydenot, T. Devillers, V. Favre-Nicolin, P. Gentile, A. Barski. *Appl. Phys. Lett.* **89**, 153129 (2006).
8. I. A. Goldthorpe, A. F. Marshall, P. C. McIntyre. *Nano Lett.* **9**, 3715 (2009).
9. L. J. Lauhon, M. S. Gudiksen, Ch. M. Lieber. *Philos. Trans. R. Soc. London, Ser. A* **362**, 1247 (2004).
10. Ch. Chen, Sh. Shehata, C. Fradin, R. LaPierre, Ch. Couteau, G. Weihs. *Nano Lett.* **7**, 2584 (2007).
11. M. J. Tambe, S. K. Lim, M. J. Smith, L. F. Allard, S. Gradecak. *Appl. Phys. Lett.* **93**, 151917 (2008).
12. M. A. Verheijen, G. Immink, Th. de Smet, M. T. Borgstrom, E. P. A. M. Bakkers. *J. Am. Chem. Soc.* **128**, 1353 (2006).
13. Ch. M. Lieber. *Nano Lett.* **2**, 81 (2002).
14. Y. Wu, R. Fan, P. Yang. *Nano Lett.* **2**, 83 (2002).
15. G. Liang, J. Xiang, N. Kharche, G. Klimeck, Ch. M. Lieber, M. Lundstrom. *Nano Lett.* **7**, 642 (2007).
16. J. Xiang, W. Lu, Y. Hu, Y. Wu, H. Yan, Ch. M. Lieber. *Nature* **441**, 489 (2006).
17. Y. Hu, J. Xiang, G. Liang, H. Yan, Ch. M. Lieber. *Nano Lett.* **8**, 925 (2008).
18. Y. Hu, H. H. Churchill, D. J. Reilly, J. Xiang, Ch. M. Lieber, Ch. M. Marcus. *Nat. Nanotechnol.* **2**, 622 (2007).
19. J.-E. Yang, Ch.-B. Jin, Ch.-J. Kim, M.-H. Jo. *Nano Lett.* **6**, 2679 (2006).
20. D. J. Paul. *Semicond. Sci. Technol.* **19**, R75 (2004).
21. R. S. Wagner, W. C. Ellis. *Appl. Phys. Lett.* **4**, 89 (1964).
22. T. B. Massalski, H. Okamoto, P. R. Subramanian, L. Kacprzak. *Binary Alloy Phase Diagrams*, ASM International, Material Park, OH (1990).
23. E. Sutter, P. Sutter. *Nano Lett.* **8**, 411 (2008).
24. D. Bahloul-Hourlier, P. Perrot. *J. Nano Res.* **4**, 135 (2008).
25. K. M. Varahramyan, D. Ferrer, E. Tutuc, S. K. Banerjee. *Appl. Phys. Lett.* **95**, 033101 (2009).
26. L. J. Lauhon, M. S. Gudiksen, D. Wang, Ch. M. Lieber. *Nature* **420**, 57 (2002).
27. Y. Zhao, J. T. Smith, J. Appenzeller, Ch. Yang. *Nano Lett.* **11**, 1406 (2011).
28. I. A. Goldthorpe, A. F. Marshall, P. C. McIntyre. *Nano Lett.* **8**, 4081 (2008).
29. H.-K. Chang, S.-Ch. Lee. *Appl. Phys. Lett.* **97**, 251912 (2010).
30. D. Briand, M. Sarret, K. Kis-Sion, T. Mohammed-Brahim, P. Duverneuil. *Semicond. Sci. Technol.* **14**, 173 (1999).

31. N. Li, T. Y. Tan, U. Gosele. *Appl. Phys. A* **90**, 591 (2008).
32. C.-Y. Wen, M. C. Reuter, J. Bruley, J. Tersoff, S. Kodambaka, E. A. Stach, F. M. Ross. *Science* **326**, 1247 (2009).
33. J. L. Lensch-Falk, E. R. Hemesath, D. E. Perea, L. J. Lauhon. *J. Mater. Chem*. **19**, 849 (2009).
34. D. E. Perea, N. Li, R. M. Dickerson, A. Misra, S. T. Picraux. *Nano Lett.* **11**, 3117 (2011).
35. A. V. Zverev, K. Yu. Zinchenko, N. L. Shwartz, Z. Sh. Yanovitskaya. *Nanotechnol. Russia* **4**, 215 (2009).
36. A. G. Nastovjak, I. G. Neizvestny, N. L. Shwartz. *Pure Appl. Chem*. **82**, 2017 (2010).
37. S. Kodambaka, J. Tersoff, M. C. Reuter, F. M. Ross. *Phys. Rev. Lett*. **96**, 096105 (2006).
38. B. Voigtlander. *Surf. Sci. Rep*. **43**, 127 (2001).
39. V. Cherepanov, B. Voigtlander. *Phys. Rev. B* **69**, 125331 (2004).
40. A. V. Zverev, I. G. Neizvestny, I. A. Reizvikh, K. N. Romanyuk, S. A. Teys, N. L. Shwartz, Z. Sh. Yanovitskaya. *Semiconductors* **39**, 967 (2005).
41. F. Glas. *Phys. Rev. B* **74**, 121302(R) (2006).
42. (a) L. Pauling. *The Nature of the Chemical Bond*, 3rd ed., Cornell University Press, Ithaca, NY (1960); (b) L. Pauling. *General Chemistry*, Dover Publications, New York (1988).